Effects of sequential decay on collective flows and nuclear stopping power in heavy-ion collisions at intermediate energies

Kui Xiao[1,2] · Peng-Cheng Li[2,3,4] · Yong-Jia Wang[2] · Fu-Hu Liu[1] · Qing-Feng Li[2,5]

Abstract

In this study, the rapidity distribution, collective flows, and nuclear stopping power in ^{197}Au+^{197}Au collisions at intermediate energies were investigated using the ultrarelativistic quantum molecular dynamics (UrQMD) model with GEMINI++ code. The UrQMD model was adopted to simulate the dynamic evolution of heavy-ion collisions, whereas the GEMINI++ code was used to simulate the decay of primary fragments produced by UrQMD. The calculated results were compared with the INDRA and FOPI experimental data. It was found that the rapidity distribution, collective flows, and nuclear stopping power were affected to a certain extent by the decay of primary fragments, especially at lower beam energies. Furthermore, the experimental data of the collective flows and nuclear stopping power at the investigated beam energies were better reproduced when the sequential decay effect was included.

Keywords Heavy-ion collisions · Sequential decay effect · Collective flow · Nuclear stopping power

1 Introduction

Understanding the properties of dense nuclear matter is a main topic of the basic research on heavy-ion collisions (HICs), as it is the only way of creating dense nuclear matter

✉ Yong-Jia Wang
wangyongjia@zjhu.edu.cn

Qing-Feng Li
liqf@zjhu.edu.cn

1 State Key Laboratory of Quantum Optics and Quantum Optics Devices and Collaborative Innovation Center of Extreme Optics, Institute of Theoretical Physics, Shanxi University, Taiyuan 030006, China

2 School of Science, Huzhou University, Huzhou 313000, China

3 School of Nuclear Science and Technology, Lanzhou University, Lanzhou 730000, China

4 Institut für Theoretische Physik, Goethe Universität Frankfurt, Frankfurt am Main 60438, Germany

5 Institute of Modern Physics, Chinese Academy of Science, Lanzhou 730000, China

in terrestrial laboratories [1–5]. However, the typical time scale for the appearance of the created dense nuclear matter is extremely short (less than or of the order of a few fm/c) [6]; thus, direct measurement of its properties is currently impossible. Usually, the fundamental properties of dense nuclear matter are inferred by comparing experimental data and transport model simulations [7–11]. As powerful tools for investigating the dynamics of nonequilibrium systems at intermediate energies, two typical transport models, the Boltzmann–Uehling–Uhlenbeck (BUU)-type [1] and quantum molecular dynamics (QMD)-type models [2] and their updated versions, have been extensively used for simulating HICs to extract the structure of the initial nuclei and the properties of the created dense nuclear matter, such as the nuclear equation of state, the nuclear symmetry energy, and the in-medium nucleon-nucleon cross section [12–17].

Both the BUU- and QMD-type models mainly include three components: the initialization of the projectile and target nuclei, mean-field potential for each particle, and two-body scattering (collision term). Different techniques are typically used to treat the three components in different models. To establish a theoretical systematic error that quantifies the model dependence of transport predictions and disentangle the causes of different predictions, the transport model evaluation project (TMEP) has been recently performed [18–22]. After simulating the dynamical process of HICs within the transport

models, an afterburner is usually chosen for the formation of fragments, which can then be used to construct observables, and further compared with the corresponding experimental data to extract interesting information regarding the nuclear matter. However, the formed fragments are typically excited and cannot be experimentally detected. In the experiments, the detected particles underwent long-term de-excitation. Hence, greater focus should be placed on the effect of de-excitation in the treatment of afterburners, especially for studying HICs at Fermi energies where the beam energy is comparable to the exciting energy [23–25].

The underestimation of the yield of light fragments (e.g., ^{3}H, ^{3}He, and ^{4}He) in HICs at intermediate energies is a long-standing problem in transport model simulations, and numerous techniques have been developed and adopted to overcome it [26], including the statistical multifragmentation model (SMM) [27, 28], the statistical evaporation model (HIVAP) [29], the statistical model GEMINI [30], and the Simulated Annealing Clusterization Algorithm (SACA) [31, 32]. From our previous studies [33–35], adopting the conventional phase space coalescence model "Minimum Spanning Tree" (MST) [36–38] and disregarding the decay of the excited primary fragments from the Ultra-relativistic Quantum Molecular Dynamics (UrQMD) model simulation, the experimental data of the collective flow of protons and deuterons at INDRA and FOPI energies can be reasonably reproduced, whereas those of α particles are different from the experimental data. To improve the corresponding collective flow distribution and explore the influence of sequential decay on the observables in the HICs at intermediate energies, the statistical code GEMINI++ was employed to describe the decay of primary fragments.

In this study, the rapidity distributions and collective flows of free protons and light clusters, as well as the nuclear stopping power, were calculated based on the UrQMD model with and without considering sequential decay. The remainder of this paper is organized as follows. In Sect. 2, the relevant descriptions of the transport model, statistical model, and the observables are provided. The calculation results are presented and discussed in Sect. 3. Finally, a summary and outlook are provided in Sect. 4.

2 Model description and observables

2.1 Dynamical model: UrQMD

The UrQMD model [39–42] is a typical transport model used for microscopic many-body nonequilibrium dynamics. In this model, each nucleon is represented by a Gaussian wave packet of a certain width L. Empirically, $L = 2$ fm^2 are chosen to simulate Au+Au collisions. The coordinates and momentum of each nucleon are propagated using Hamilton's equations of motion. The total Hamiltonian of the system $\langle H \rangle$ consists of the kinetic energy T and the effective interaction potential energy U, which includes the Skyrme potential energy U_ρ, Coulomb energy U_{Coul}, and momentum-dependent potential energy U_{md}:

$$\langle H \rangle = T + U_\rho + U_{\text{Coul}} + U_{\text{md}}. \tag{1}$$

To study the HICs at intermediate energies, the Skyrme energy density functional was introduced in the same manner as that in the improved quantum molecular dynamics (ImQMD) model [43, 44]. The local and momentum-dependent potential energies can be written as $U_{\rho,\text{md}} = \int u_{\rho,\text{md}} d\mathbf{r}$, where

$$u_\rho = \frac{\alpha}{2} \frac{\rho^2}{\rho_0} + \frac{\beta}{\gamma + 1} \frac{\rho^{\gamma+1}}{\rho_0^\gamma} + \frac{g_{\text{sur}}}{2\rho_0} (\nabla \rho)^2$$
$$+ \frac{g_{\text{sur,iso}}}{2\rho_0} \left[\nabla (\rho_n - \rho_p) \right]^2$$
$$+ \left[A_{\text{sym}} \left(\frac{\rho}{\rho_0} \right) + B_{\text{sym}} \left(\frac{\rho}{\rho_0} \right)^\eta + C_{\text{sym}} \left(\frac{\rho}{\rho_0} \right)^{5/3} \right] \delta^2 \rho, \tag{2}$$

and

$$u_{\text{md}} = t_{\text{md}} \ln^2 \left[1 + a_{\text{md}} (\mathbf{p}_i - \mathbf{p}_j)^2 \right] \frac{\rho}{\rho_0}. \tag{3}$$

Here, $\delta = (\rho_n - \rho_p)/(\rho_n + \rho_p)$ denotes the isospin asymmetry defined by the neutron (ρ_n) and proton (ρ_p) densities. In the present work, the normal nuclear matter density $\rho_0 = 0.16$ fm^{-3}, $\alpha = -393$ MeV, $\beta = 320$ MeV, $\gamma = 1.14$, $g_{\text{sur}} = 19.5$ MeV fm^2, $g_{\text{sur,iso}} = -11.3$ MeV fm^2, $A_{\text{sym}} = 20.4$ MeV, $B_{\text{sym}} = 10.8$ MeV, $C_{\text{sym}} = -9.3$ MeV, $\eta = 1.3$, $t_{\text{md}} = 1.57$ MeV, and $a_{\text{md}} = 500$ (GeV/c)$^{-2}$ are chosen, corresponding to a soft and momentum-dependent (SM) equation of state with the incompressibility $K_0 = 200$ MeV and the symmetry-energy slope parameter $L = 80.95$ MeV, which are in their commonly accepted regions [42, 45–49].

In this work, the in-medium nucleon-nucleon (NN) elastic cross section is considered as the result of a density- and momentum-dependent medium correction factor $\mathcal{F}(\rho, p)$ times the free nucleon-nucleon cross section $\sigma_{\text{NN}}^{\text{free}}$, which is available from the experimental data.

$$\sigma_{\text{NN}}^{\text{in-medium}} = \mathcal{F}(\rho, p) * \sigma_{\text{NN}}^{\text{free}}, \tag{4}$$

with

$$\mathcal{F}(\rho, p) = \begin{cases} f_0, & p_{\text{NN}} > 1 \text{GeV}/c, \\ \frac{\lambda + (1-\lambda)e^{-\frac{\rho}{\zeta\rho_0}} - f_0}{1 + (p_{\text{NN}}/p_0)^\kappa} + f_0, & p_{\text{NN}} \leq 1 \text{GeV}/c. \end{cases} \tag{5}$$

The parameters $f_0 = 1$, $\lambda = 1/6$, $\zeta = 1/3$, $p_0 = 0.3$ GeV/c, and $\kappa = 8$ were adopted, with p_{NN} being the momentum in the two-nucleon center-of-mass frame. More detailed

studies regarding the effects of $\mathcal{F}(\rho, p)$ parameters on various observables can be found in Refs. [41, 42, 50]. In addition to the in-medium NN cross section, Pauli blocking plays an important role in determining the rate of collisions. The Pauli blocking treatment is the same as that described in Refs. [19, 41]; it involves two steps. First, the phase space densities f_i and f_j of the two outgoing particles for each NN collision are calculated.

$$f_i = \frac{1}{2} \sum_k \frac{1}{(\pi \hbar)^3} \exp\left[-\frac{(\mathbf{r}_i - \mathbf{r}_k)^2}{(2\sigma_r^2)}\right]$$
$$\exp\left[-\frac{(\mathbf{p}_i - \mathbf{p}_k)^2 \cdot 2\sigma_r^2}{\hbar^2}\right]. \tag{6}$$

Here, σ_r^2 denotes the width parameter of the wave packet. $\sigma_r^2 = 2 \text{ fm}^2$ is used in this study. k represents the nucleons of the same type around the outgoing nucleon i (or j). The following two criteria were simultaneously considered:

$$\frac{4\pi}{3} r_{ik}^3 \frac{4\pi}{3} p_{ik}^3 \geq 2\left(\frac{h}{2}\right)^3; \tag{7}$$

$$P_{\text{block}} = 1 - (1 - f_i)(1 - f_j) < \xi. \tag{8}$$

Here, r_{ik} and p_{ik} denote the relative distance and momentum between the nucleons i and k. The above conditions were also considered for nucleon j. The symbol ξ denotes a random number between 0 and 1.

In addition, the isospin-dependent minimum spanning tree (iso-MST) algorithm was used to construct the clusters [36–38]. Nucleon pairs with relative distances smaller than R_0 and relative momenta smaller than $P_0 = 0.25 \text{ GeV}/c$ are considered to be bound in a fragment. Here, $R_0^{\text{pp}} = 2.8 \text{ fm}$ and $R_0^{\text{np}} = R_0^{\text{nn}} = 3.8 \text{ fm}$ were used for proton-proton and neutron-neutron (neutron-proton) pairs, respectively. A fairly good agreement between the recently published experimental data (including collective flows, nuclear stopping power, and Hanbury–Brown–Twiss interferometry) and UrQMD model calculations was achieved with appropriate choices of the above parameters [35, 42, 45, 51, 52].

2.2 Statistical model: GEMINI++

The statistical GEMINI++ decay model [30, 53] is a Monte Carlo method used to simulate the decay of excited fragments, which includes light-particle evaporation, symmetric and asymmetric fission, and all possible binary decay modes. It has been widely used to treat the de-excitation of the primary fragments in studies of nuclear reactions at low and intermediate [23, 25, 54–60] and high energies [61–63]. The parameters of the shell-smoothed level density in GEMINI++ were set to their default values, which were $k_0 = 7.3 \text{ MeV}$ and

$k_\infty = 12 \text{ MeV}$. A more detailed discussion of the GEMINI++ parameters can be found in Refs. [53, 60, 64].

There are four inputs for the GEMINI++ code (with default parameter settings): the mass number A, charge number Z, excitation energy E^*, and angular moment $\vec{L}$ of the primary fragment. After the UrQMD transport and iso-MST coalescence processes, the excitation energy of a fragment is calculated as follows:

$$E^* = E_{\text{bind}}^{\text{excited}} - E_{\text{bind}}^{\text{ground}}, \tag{9}$$

where $E_{\text{bind}}^{\text{excited}}$ is the binding energy of the primary fragment, that is, the sum of the potential and kinetic energies of all nucleons that belong to a fragment. $E_{\text{bind}}^{\text{ground}}$ is the binding energy of the ground state obtained from nuclear data table AME2020 [65, 66]. When the excitation energy of the fragment was less than or equal to zero, it was regarded as a bound state and did not decay further. The angular momentum of the primary fragments was calculated using classical mechanics [56].

$$\vec{L} = \sum_i \vec{r}_i \times \vec{p}_i, \tag{10}$$

where $\vec{r}_i$ and $\vec{p}_i$ are the coordinate and momentum vectors, respectively, of the i-th nucleon in the primary fragments in the c.m. frame of the fragment. The total angular momentum is the sum of all the nucleons in the primary fragments. We verified that the results remained almost unchanged if the contribution of the angular momentum in GEMINI++ was not included.

2.3 Observables

In this study, we focus on collective flows and nuclear stopping power, which are commonly used observables, and propose investigating the properties of dense nuclear matter. The directed (v_1) and elliptic (v_2) flows are defined as [67]

$$v_1 = \left\langle \frac{p_x}{\sqrt{p_x^2 + p_y^2}} \right\rangle, \quad v_2 = \left\langle \frac{p_x^2 - p_y^2}{\sqrt{p_x^2 + p_y^2}} \right\rangle. \tag{11}$$

Here, p_x and p_y are the two components of the transverse momentum $p_t = \sqrt{p_x^2 + p_y^2}$. Angle brackets indicate the average of all considered particles from all events. The nuclear stopping power R_E, which characterizes the transparency of the colliding nuclei, can be defined as [68]

$$R_E = \frac{\sum E_\perp}{2 \sum E_\parallel}, \tag{12}$$

where $E_\perp$ ($E_\parallel$) is the c.m. transverse (parallel) energy, and the sum runs over all considered particles. Another quantity *vartl*, which was proposed by the FOPI Collaboration [69], is widely used to measure stopping power. It is defined as

the ratio of the variances of the transverse to those of the longitudinal rapidity distribution and is expressed as

$$vartl = \frac{\langle y_x^2 \rangle}{\langle y_z^2 \rangle}, \tag{13}$$

where $\langle y_x^2 \rangle$ and $\langle y_z^2 \rangle$ are the variances in the rapidity distributions of the particles in the x and z directions, respectively.

3 Results and discussions

3.1 Rapidity distribution

The rapidity distributions of hydrogen ($Z = 1$) and helium isotopes (^{3}He and ^{4}He) in ^{197}Au+^{197}Au collisions at $E_{lab} = 40$ MeV/nucleon and impact parameter $b = 5.5$–7.5 fm are shown in Fig. 1. The left, middle, and right panels show the calculated results when the switching time of the UrQMD model was set to 200, 250, and 300 fm/c, respectively. When considering the decay of the excited primary fragments, the yields of $Z = 1$ particles are slightly increased, whereas those of ^{3}He and ^{4}He clusters are clearly increased. The yields of ^{3}He and ^{4}He are approximately 1.5 and 6 times greater than those obtained from the simulations without considering sequential decay. It is known that the yields of light clusters such as ^{3}He and ^{4}He obtained using QMD-type codes are significantly smaller than experimentally measured yields. As discussed in our previous work [44], the yield of ^{3}He calculated using the UrQMD model was approximately three times lower than that of the experimental data. The inclusion of GEMINI++ improved the description of light cluster production to some extent; however, the yields of light clusters were still underestimated. Additionally, the inclusion of GEMINI++ may have led to an overestimation of the yield of free nucleons. To solve these problems further, additional issues should be considered, such as the spin degree of freedom and the dynamical production process [7].

3.2 Collective flows

The collective flows of $Z = 1$ particles as functions of y_0 in ^{197}Au+^{197}Au collisions at $E_{lab} = 40$ MeV/nucleon are shown in Fig. 2 (directed flow v_1 [left panel] and elliptic flow v_2 [right panel]). The simulations were terminated at 200 fm/c. Clear differences are observed in the distributions of the collective flows between simulations with and without considering the decay of the primary fragments, especially in the case of elliptic flow v_2 from peripheral ($b = 5.5$–7.5 fm)
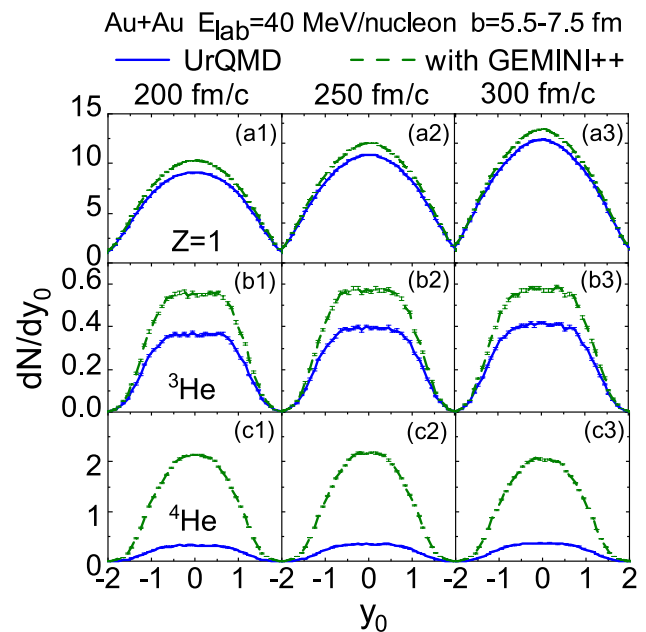

Fig. 1 (Color online) Rapidity distributions of $Z = 1$ [panels (a1–a3)], ^{3}He [panels (b1–b3)], and ^{4}He [panels (c1–c3)] particles as functions of the reduced rapidities ($y_0 = y_z/y_{pro}$) from peripheral ($b = 5.5$–7.5 fm) ^{197}Au+^{197}Au collisions at $E_{lab} = 40$ MeV/nucleon at different reaction times. The solid and dashed lines represent the results obtained from UrQMD simulations with and without considering the decay of the primary fragments using GEMINI++, respectively
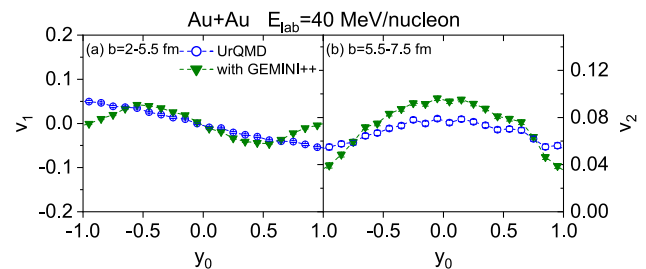

Fig. 2 (Color online) Reduced rapidity y_0 distributions of the directed (elliptic) flow v_1 (v_2) from semi-central (peripheral) ^{197}Au+^{197}Au collisions at $E_{lab} = 40$ MeV/nucleon for $Z = 1$ particles. The blue circles denote the calculated results without primary fragment decay, whereas the olive down-triangles represent the calculated results with primary fragments de-excited

collisions. From Fig. 1, the difference in the yields of $Z = 1$ particles between simulations with and without considering sequential decay is due to the particles produced from the decay of excited primary fragments, which have larger mass. These heavier excited primary fragments are usually produced at the target/projectile rapidity; thus, the directed flow at the target/projectile rapidity is significantly affected by sequential decay. Increasing the impact parameter results in more large-mass primary fragments being produced and the

effects of sequential decay on the collective flows becoming more evident.

To quantitatively evaluate the influence of sequential decay on the collective flows, as shown in Fig. 3, the v_1 slope (top panels) and v_2 (bottom panels) at mid-rapidity for $Z = 1$ particles (left panels) and free protons (right panels) are calculated at different stopping times and compared with the experimental data. The slope of directed flow v_{11} and elliptic flow v_{20} at mid-rapidity are extracted by assuming $v_1(y_0) = v_{10} + v_{11} \cdot y_0 + v_{13} \cdot y_0^3$ and $v_2(y_0) = v_{20} + v_{22} \cdot y_0^2 + v_{24} \cdot y_0^4$ in the range of $|y_0| < 0.4$, in the same manner as that in the experimental report [69–71]. The left panels show the results from the simulations at $E_{\text{lab}} = 50$ MeV/nucleon, whereas the right panels show the results from the simulations at $E_{\text{lab}} = 400$ MeV/nucleon. There is an obvious difference in v_{11} and v_{20} between the simulations with and without considering the decay of primary fragments at $E_{\text{lab}} = 50$ MeV/nucleon. By considering the decay of the primary fragments, the value of v_{11} decreases, while that of v_{20} increases, and both are closer to the experimental data. This can be understood from the fact that both directed and elliptic flows are stronger for large-mass fragments [33, 69, 70]. The decay of fragments is isotropic within the fragments c.m. in the statistical model. Thus, the light nuclei produced from the decay of primary fragments retain information about the primary fragments. Furthermore, at $E_{\text{lab}} = 50$ MeV/nucleon, v_{11} first decreases with time and then saturates (increases) after 200 fm/c in the case without (with) the sequential decay effect. This can be explained by the competition between sequential decay and dynamical effects. At approximately $t = 150$ fm/c, the nucleons are located in a low-density environment, and the final state interactions are attractive; thus, a decrease
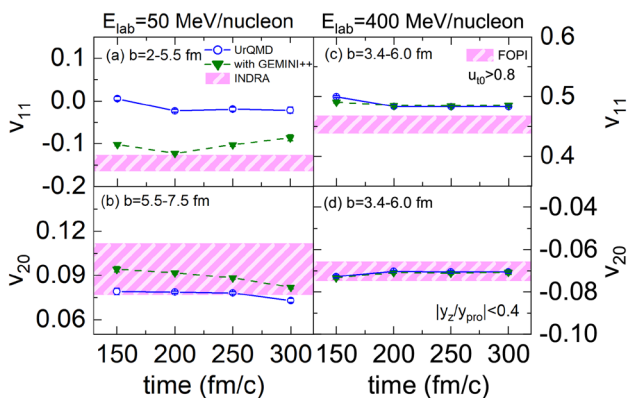

Fig. 4 (Color online) Beam energy dependence of directed flow slope v_{11} (panel a) and elliptic flow v_{20} (panel b) from semi-central ^{197}Au+^{197}Au collisions. As shown, the solid stars represent the data from INDRA Collaboration [70] for $Z = 1$ particles, and the open stars are the results from FOPI Collaboration [69, 71] for free protons with $u_{t0} > 0.8$ cut. The lines with different symbols are the results of calculations with and without considering the sequential decay. Where error bars are not shown, they fall within the symbols

Fig. 3 (Color online) Directed flow slope v_{11} and elliptic flow v_{20} from ^{197}Au+^{197}Au collisions at $E_{\text{lab}} = 50$ MeV/nucleon (for hydrogen isotopes ($Z = 1$)) and 400 MeV/nucleon (for free protons with $u_{t0} > 0.8$) with different stopping times. The INDRA and FOPI experimental data taken from Refs. [69–71] are indicated by shaded bands
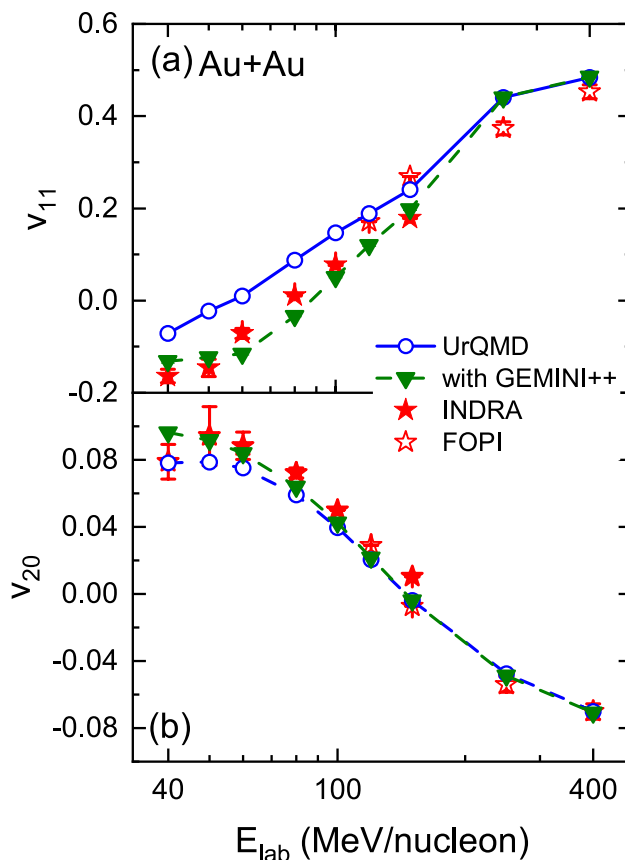
v_{11} is observed. When considering GEMINI++ at $t = 300$ fm/c, there are only a few large-mass fragments that can emit hydrogen isotopes, and the effect of sequential decay on v_{11} gradually weakens. A comparison of the sequential decay effects at $E_{\text{lab}} = 50$ MeV/nucleon with those at $E_{\text{lab}} = 400$ MeV/nucleon shows that the sequential decay effects are more pronounced at lower beam energies. This is understandable because more large-mass fragments, which contribute to the production of light clusters, are formed at lower beam energies.

Figure 4 shows the beam energy dependence of v_{11} (top panel) and v_{20} (bottom panel) for semi-central ^{197}Au+^{197}Au collisions. The value of v_{11} from the simulations without considering sequential decay is higher than that of the experimental data at lower energies. When sequential decay is included, v_{11} is driven down, and v_{20} is pulled up at low energies, which is consistent with the results shown in Fig. 3. Again, both v_{11} and v_{20} are considerably closer to

the experimental data for all investigated energies. Moreover, the effects of sequential decay on the collective flows decrease with increasing beam energy. With increasing beam energy, the reaction becomes more violent, and the multiplicities of large-mass primary fragments decrease.

For a systematic investigation of the effects of sequential decay on the collective flows, the transverse 4-velocities u_{t0} dependence of the v_1 of light charged particles in semi-central ^{197}Au+^{197}Au collisions at $E_{lab} = 120, 150$, and 250 MeV/nucleon are calculated with and without considering the decay of primary fragments and compared with the experimental data [69], as shown in Fig. 5. The effects of sequential decay on v_1 (u_{t0}) of particles with mass number $A < 4$ are relatively weak; it only affects v_1 at low u_{t0}. By considering the sequential decay effect, v_1 of α particles is obviously influenced and can reproduce the experimental data reasonably well at higher u_{t0}. This is because after the decay of excited primary fragments is considered, the multiplicity of α particles is enhanced, as shown in Fig. 1. The α particles produced by the decay of the excited primary fragments have a large flow effect because they inherit the flow information of the excited primary fragments. The remaining discrepancies in u_{t0}-dependent v_1 of light clusters may be due to simplifications in the initial wave function of particles (nucleons and possible clusters) and quantum effects in two-body collisions, as well as the lack of a dynamical production process, which requires further study [7].

3.3 Nuclear stopping power

The nuclear stopping power characterizes the transparency of the colliding nuclei and can provide insight into the rate of equilibration of the colliding system. Thus, it is meaningful to explore the effects of sequential decay on the nuclear stopping power. The yield distributions of deuterons and ^{4}He clusters as functions of the reduced longitudinal (y_z/y_{pro}) and transverse (y_x/y_{pro}) rapidities for central ^{197}Au+^{197}Au collisions at $E_{lab} = 40$ MeV/nucleon with and without considering sequential decay are shown in Fig. 6. The values of the calculated R_E are shown in each panel, and they slightly decrease; that is, the nuclear stopping power is depressed when considering the sequential decay. Notably, the values of R_E are slightly influenced by sequential decay; however, the yield spectrum of each particle is obviously influenced, especially for ^{4}He clusters. In conjunction with the results presented in Fig. 1, it can be concluded that sequential decay has a strong effect on the particle yield and yield distribution; however, the nuclear stopping power is only weakly influenced because the de-excitation of the primary fragments in the GEMINI++ code is isotropic.

The nuclear stopping power R_E ($E_{lab} = 40$ MeV/nucleon, left panel) and *vartl* ($E_{lab} = 400$ MeV/nucleon, right panel) for free protons from central ($b = 0$–2 fm) ^{197}Au+^{197}Au collisions calculated at different stopping times are shown in Fig. 7. Similar to the collective flows shown in Fig. 3, the effects of sequential decay on the nuclear stopping power at lower energies are more obvious than those at higher

Fig. 5 (Color online) Directed flow v_1 of protons (squares), deuterons (circles), $A = 3$ clusters (triangles), and α-particles (rhombuses) versus u_{t0} in ^{197}Au+^{197}Au collisions at $E_{lab} = 120, 150$, and 250 MeV/nucleon with $b = 3.4$–6.0 fm. Results from calculations with
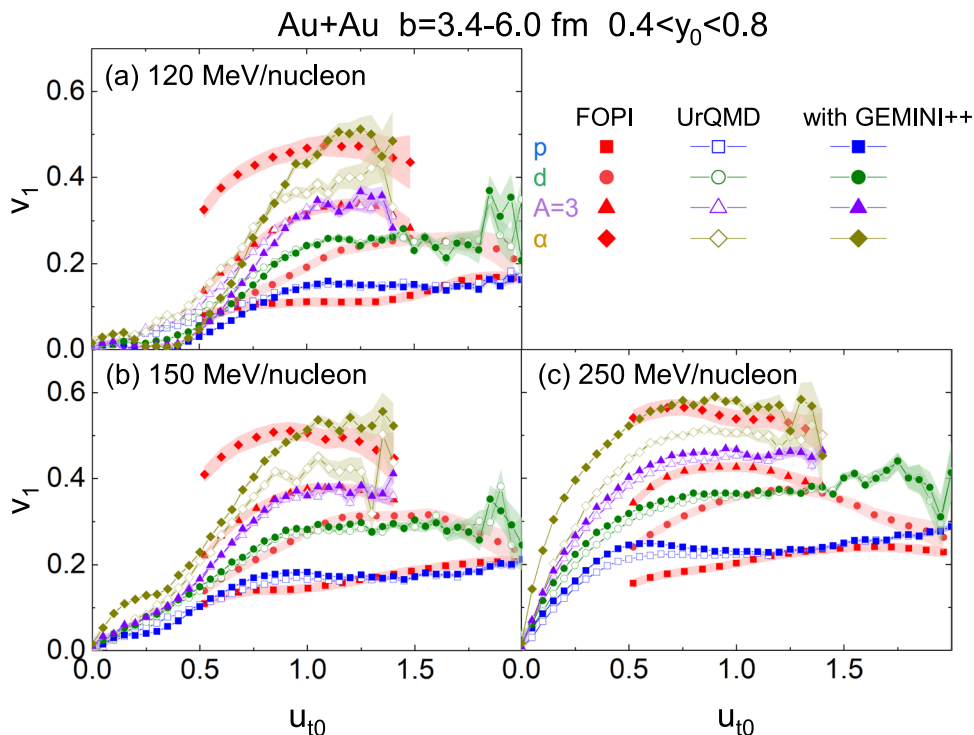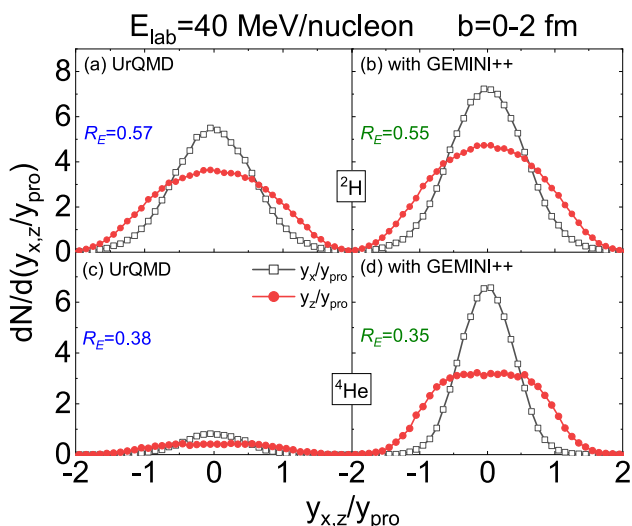
Fig. 6 (Color online) Yield distributions of ^{2}H and ^{4}He particles as functions of the reduced longitudinal and transverse rapidities from central ($b = 0$–2 fm) ^{197}Au+^{197}Au collisions at $E_{lab} = 40$ MeV/nucleon. Results from calculations with and without the sequential decay are shown in the left and right panels, respectively. The corresponding values for nuclear stopping power R_E are also indicated in each panel

energies. In all cases, the results were saturated and were close to or covered by the experimental data above 200 fm/c.

Figure 8 shows the degree of nuclear stopping (R_E or *vartl*) in the central ^{197}Au+^{197}Au collisions as a function of the beam energy. It is clear that both R_E and *vartl* decrease and are much closer to the experimental data when the GEMINI++ code is applied, and the difference in the values of the nuclear stopping power gradually disappears with increasing beam energy. With the same impact parameter (centrality), more violent reactions occurred at higher beam
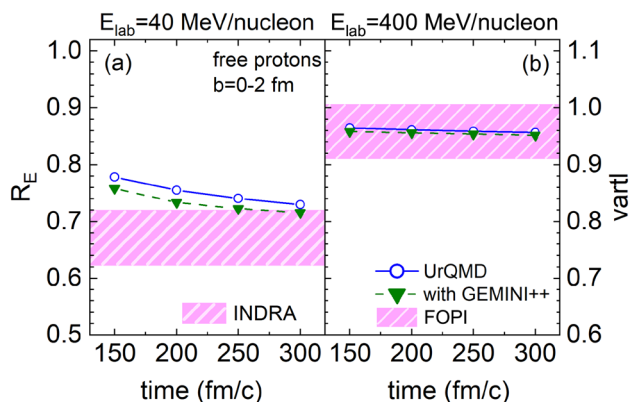
energies, and less heavily excited primary fragments were produced. The difference with free protons is that they are produced from the decay of heavy excited primary fragments, which usually have a weak stopping power (smaller values of R_E and *vartl*) [73, 74]. As a result, the nuclear stopping power was slightly reduced by including the GEMINI++ code.

4 Summary and outlook

In summary, the effects of the sequential decay of excited primary fragments on the rapidity distribution, collective flows of light nuclei, and nuclear stopping power in Au+Au collisions at intermediate energies were investigated. Primary fragments were produced using the UrQMD model, and sequential decay of the excited primary fragments was performed using the GEMINI++ code. It was observed that the sequential decay of the excited primary fragments have an obvious influence on the rapidity distribution and collective flows but relatively weakly affect the stopping power. This is because of the memory effect; that is, the light particles produced from the sequential decay of the excited primary fragments inherit the collective properties of the excited primary fragments. Furthermore, the sequential decay effects gradually decreased with increasing beam energy because fewer large-mass fragments that can emit light particles were produced at higher beam energies. More importantly, the ability to reproduce the relevant experimental data at the investigated energies was improved to a certain extent by the inclusion of sequential decay effects.
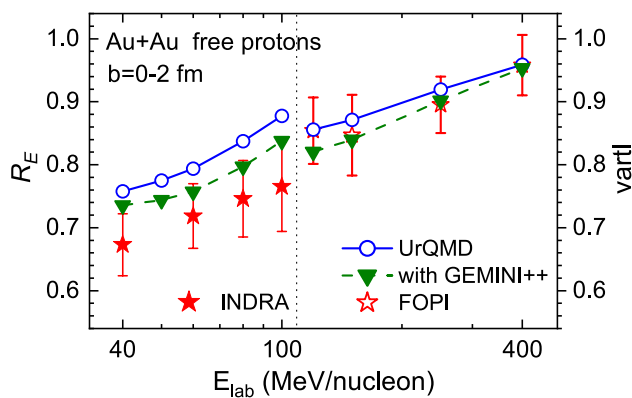

Fig. 7 (Color online) R_E and *vartl* for free protons from central ($b = 0$–2 fm) ^{197}Au+^{197}Au collisions with $E_{lab} = 40$ and 400 MeV/nucleon at different stopping times. The symbols sets are identical to those in Fig. 1. The shaded bands are the corresponding INDRA and FOPI experimental data taken from Refs. [72, 73]

Fig. 8 (Color online) Beam-energy dependence of R_E (INDRA) and *vartl* (FOPI) for free protons from central ($b = 0$–2 fm) ^{197}Au+^{197}Au collisions. The symbols sets are identical to those in Fig. 5. Calculations with and without sequential decay are compared with the INDRA and FOPI experimental data, which are taken from Refs. [72, 73], respectively

These results are meaningful for extracting the properties of nuclear matter by comparing transport model calculations with experimental data. The effects of secondary sequential decay on the observables, such as the *N/Z* ratios and elliptic flow ratios of neutrons vs. hydrogen isotopes, will be discussed in future publications.

References

1. G.F. Bertsch, S. Das Gupta, A Guide to microscopic models for intermediate-energy heavy ion collisions. Phys. Rept. **160**, 189–233 (1988). https://doi.org/10.1016/0370-1573(88)90170-6

2. J. Aichelin, Quantum molecular dynamics: a dynamical microscopic n body approach to investigate fragment formation and the nuclear equation of state in heavy ion collisions. Phys. Rept. **202**, 233–360 (1991). https://doi.org/10.1016/0370-1573(91)90094-3

3. P. Danielewicz, R. Lacey, W.G. Lynch, Determination of the equation of state of dense matter. Science **298**, 1592–1596 (2002). https://doi.org/10.1126/science.1078070

4. B.A. Li, L.W. Chen, C.M. Ko, Recent progress and new challenges in isospin physics with heavy-ion reactions. Phys. Rep. **464**, 113–281 (2008). https://doi.org/10.1016/j.physrep.2008.04.005

5. J. Xu, Transport approaches for the description of intermediate-energy heavy-ion collisions. Prog. Part. Nucl. Phys. **106**, 312–359 (2019). https://doi.org/10.1016/j.ppnp.2019.02.009

6. D. Guo, Y.H. Qin, S. Xiao et al., An FPGA-based trigger system for CSHINE. Nucl. Sci. Tech. **33**, 162 (2022). https://doi.org/10.1007/s41365-022-01149-0

7. A. Ono, Dynamics of clusters and fragments in heavy-ion collisions. Prog. Part. Nucl. Phys. **105**, 139–179 (2019). https://doi.org/10.1016/j.ppnp.2018.11.001

8. M. Bleicher, E. Bratkovskaya, Modelling relativistic heavy-ion collisions with dynamical transport approaches. Prog. Part. Nucl. Phys. **122**, 103920 (2022). https://doi.org/10.1016/j.ppnp.2021.103920

9. M. Colonna, Collision dynamics at medium and relativistic energies. Prog. Part. Nucl. Phys. **113**, 103775 (2020). https://doi.org/10.1016/j.ppnp.2020.103775

10. S. Huth, P.T. Pang, I. Tews et al., Constraining neutron-star matter with microscopic and macroscopic collisions. Nature **606**, 276–280 (2022). https://doi.org/10.1038/s41586-022-04750-w

11. S.W. Lan, S.S. Shi, Anisotropic flow in high baryon density region. Nucl. Sci. Tech. **33**, 21 (2022). https://doi.org/10.1007/s41365-022-01006-0

12. C.Z. Shi, Y.G. Ma, α-clustering effect on flows of direct photons in heavy-ion collisions. Nucl. Sci. Tech. **32**, 66 (2021). https://doi.org/10.1007/s41365-021-00897-9

13. Z.W. Lin, L. Zheng, Further developments of a multiphase transport model for relativistic nuclear collisions. Nucl. Sci. Tech. **32**, 113 (2021). https://doi.org/10.1007/s41365-021-00944-5

14. H. Wang, J.H. Chen, Study on open charm hadron production and angular correlation in high-energy nuclear collisions. Nucl. Sci. Tech. **32**, 2 (2021). https://doi.org/10.1007/s41365-020-00839-x

15. Y.J. Wang, F.-H. Guan, X.-Y. Diao et al., CSHINE for studies of HBT correlation in heavy ion reactions. Nucl. Sci. Tech. **32**, 4 (2021). https://doi.org/10.1007/s41365-020-00842-2

16. C. Liu, X.G. Deng, Y.G. Ma, Density fluctuations in intermediate-energy heavy-ion collisions. Nucl. Sci. Tech. **33**, 52 (2022). https://doi.org/10.1007/s41365-022-01040-y

17. R.S. Wang, L. Ou, Z.G. Xiao, Production of high-energy neutron beam from deuteron breakup. Nucl. Sci. Tech. **33**, 92 (2022). https://doi.org/10.1007/s41365-022-01075-1

18. J. Xu, L.W. Chen, M.B. Tsang et al., Understanding transport simulations of heavy-ion collisions at 100 A and 400A MeV: comparison of heavy-ion transport codes under controlled conditions. Phys. Rev. C **93**, 044609 (2016). https://doi.org/10.1103/PhysRevC.93.044609

19. H. Wolter, M. Colonna, D. Cozma et al., Transport model comparison studies of intermediate-energy heavy-ion collisions. Prog. Part. Nucl. Phys. **125**, 103962 (2022). https://doi.org/10.1016/j.ppnp.2022.103962

20. M. Colonna, Y.X. Zhang, Y.J. Wang et al., Comparison of heavy-ion transport simulations: mean-field dynamics in a box. Phys. Rev. C **104**, 024603 (2021). https://doi.org/10.1103/PhysRevC.104.024603

21. A. Ono, J. Xu, M. Colonna et al., Comparison of heavy-ion transport simulations: collision integral with pions and Δ resonances in a box. Phys. Rev. C **100**, 044617 (2019). https://doi.org/10.1103/PhysRevC.100.044617

22. Y.X. Zhang, Y.J. Wang, M. Colonna et al., Comparison of heavy-ion transport simulations: collision integral in a box. Phys. Rev. C **97**, 034625 (2018). https://doi.org/10.1103/PhysRevC.97.034625

23. W.D. Tian, Y.G. Ma, X.Z. Cai et al., Dynamical and sequential decay effects on isoscaling and density dependence of the symmetry energy. Int. J. Mod. Phys. E **17**, 1705–1719 (2008). https://doi.org/10.1142/S0218301308010714

24. J. Su, W. Trautmann, L. Zhu et al., Dynamical properties and secondary decay effects of projectile fragmentations in Sn124, Sn107+Sn120 collisions at 600 MeV/nucleon. Phys. Rev. C **98**, 014610 (2018). https://doi.org/10.1103/PhysRevC.98.014610

25. C.C. Guo, J. Su, L. Zhu, Secondary decay effects of the isospin fractionation in the projectile fragmentation at GeV/nucleon. Nucl. Sci. Tech. **31**, 123 (2020). https://doi.org/10.1007/s41365-020-00832-4

26. M.B. Tsang, R. Bougault, R. Charity et al., Comparisons of statistical multifragmentation and evaporation models for heavy ion

collisions. Eur. Phys. J. A **30**, 129–139 (2006). https://doi.org/10.1140/epja/i2007-10389-2

27. J.P. Bondorf, R. Donangelo, I.N. Mishustin et al., Statistical multifragmentation of nuclei. Nucl. Phys. A **443**, 321–347 (1985). https://doi.org/10.1016/0375-9474(85)90266-0

28. J.P. Bondorf, A.S. Botvina, A.S. Ilinov et al., Statistical multifragmentation of nuclei. Phys. Rept. **257**, 133–221 (1995). https://doi.org/10.1016/0370-1573(94)00097-M

29. W. Reisdorf, Analysis of fissionability data at high excitation energies. Z. Phys. A Atoms Nuclei **300**, 227–238 (1981). https://doi.org/10.1007/BF01412298

30. R.J. Charity, M.A. McMahan, G.J. Wozniak et al., Systematics of complex fragment emission in niobium-induced reactions. Nucl. Phys. A **483**, 371–405 (1988). https://doi.org/10.1016/0375-9474(88)90542-8

31. R.K. Puri, C. Hartnack, J. Aichelin, Early fragment formation in heavy ion collisions. Phys. Rev. C **54**, R28–R31 (1996). https://doi.org/10.1103/PhysRevC.54.R28

32. R.K. Puri, J. Aichelin, Simulated annealing clusterization algorithm for studying the multifragmentation. J. Comput. Phys. **162**, 245–266 (2000). https://doi.org/10.1006/jcph.2000.6534

33. Y. Wang, C. Guo, Q. Li et al., Collective flows of light particles in the Au+Au collisions at intermediate energies. Phys. Rev. C **89**, 034606 (2014). https://doi.org/10.1103/PhysRevC.89.034606

34. P.C. Li, Y.J. Wang, Q.F. Li et al., Collective flow and nuclear stopping in heavy ion collisions in Fermi energy domain. Nucl. Sci. Tech. **29**, 177 (2018). https://doi.org/10.1007/s41365-018-0510-1

35. P. Li, Y. Wang, Q. Li et al., Accessing the in-medium effects on nucleon-nucleon elastic cross section with collective flows and nuclear stopping. Phys. Lett. B **828**, 137019 (2022). https://doi.org/10.1016/j.physletb.2022.137019

36. Q. Li, Y. Wang, X. Wang et al., Influence of coalescence parameters on the production of protons and Helium-3 fragments. Sci. China Phys. Mech. Astron. **59**, 672013 (2016). https://doi.org/10.1007/s11433-016-0120-3

37. Q. Li, Y. Wang, X. Wang et al., Helium-3 production from Pb+Pb collisions at SPS energies with the UrQMD model and the traditional coalescence afterburner. Sci. China Phys. Mech. Astron. **59**, 632002 (2016). https://doi.org/10.1007/s11433-015-5775-3

38. Q. Li, Y. Wang, X. Wang et al., Rapidity distribution of protons from the potential version of UrQMD model and the traditional coalescence afterburner. Sci. China Phys. Mech. Astron. **59**, 622001 (2016). https://doi.org/10.1007/s11433-015-5768-2

39. S.A. Bass, M. Belkacem, M. Bleicher et al., Microscopic models for ultrarelativistic heavy ion collisions. Prog. Part. Nucl. Phys. **41**, 255–369 (1998). https://doi.org/10.1016/S0146-6410(98)00058-1

40. M. Bleicher, E. Zabrodin, C. Spieles et al., Relativistic hadron hadron collisions in the ultrarelativistic quantum molecular dynamics model. J. Phys. G **25**, 1859–1896 (1999). https://doi.org/10.1088/0954-3899/25/9/308

41. Q. Li, C. Shen, C. Guo et al., Nonequilibrium dynamics in heavy-ion collisions at low energies available at the GSI Schwerionen Synchrotron. Phys. Rev. C **83**, 044617 (2011). https://doi.org/10.1103/PhysRevC.83.044617

42. Y.J. Wang, Q.F. Li, Application of microscopic transport model in the study of nuclear equation of state from heavy ion collisions at intermediate energies. Front. Phys. (Beijing) **15**, 44302 (2020). https://doi.org/10.1007/s11467-020-0964-6

43. Y. Zhang, N. Wang, Q.F. Li et al., Progress of quantum molecular dynamics model and its applications in heavy ion collisions. Front. Phys. (Beijing) **15**, 54301 (2020). https://doi.org/10.1007/s11467-020-0961-9

44. Y. Wang, C. Guo, Q. Li et al., ^{3}H/^{3}He ratio as a probe of the nuclear symmetry energy at sub-saturation densities. Eur. Phys. J. A **51**, 37 (2015). https://doi.org/10.1140/epja/i2015-15037-8

45. Y. Wang, C. Guo, Q. Li et al., Determination of the nuclear incompressibility from the rapidity-dependent elliptic flow in heavy-ion collisions at beam energies 0.4 A – 1.0 A GeV. Phys. Lett. B **778**, 207–212 (2018). https://doi.org/10.1016/j.physletb.2018.01.035

46. J.F. Xu, C.J. Xia, Z.Y. Lu et al., Symmetry energy of strange quark matter and tidal deformability of strange quark stars. Nucl. Sci. Tech. **33**, 143 (2022). https://doi.org/10.1007/s41365-022-01130-x

47. G.F. Wei, X. Huang, Q.J. Zhi et al., Effects of the momentum dependence of nuclear symmetry potential on pion observables in Sn + Sn collisions at 270 MeV/nucleon. Nucl. Sci. Tech. **33**, 163 (2022). https://doi.org/10.1007/s41365-022-01146-3

48. J. Liu, C. Gao, N. Wan et al., Basic quantities of the equation of state in isospin asymmetric nuclear matter. Nucl. Sci. Tech. **32**, 117 (2021). https://doi.org/10.1007/s41365-021-00955-2

49. Y. Wang, Q. Li, Y. Leifels et al., Study of the nuclear symmetry energy from the rapidity-dependent elliptic flow in heavy-ion collisions around 1 GeV/nucleon regime. Phys. Lett. B **802**, 135249 (2020). https://doi.org/10.1016/j.physletb.2020.135249

50. P. Li, Y. Wang, Q. Li et al., Effects of the in-medium nucleon-nucleon cross section on collective flow and nuclear stopping in heavy-ion collisions in the Fermi-energy domain. Phys. Rev. C **97**, 044620 (2018). https://doi.org/10.1103/PhysRevC.97.044620

51. P. Li, Y. Wang, Q. Li et al., Transport model analysis of the pion interferometry in au+au collisions at e_{beam}=1.23 gev/nucleon. SCIENCE CHINA Physics. Mech. Astron. **66**, 222011 (2023). https://doi.org/10.1007/s11433-022-2026-5

52. P. Li, J. Steinheimer, T. Reichert et al., Effects of a phase transition on two-pion interferometry in heavy ion collisions at $\sqrt{s_{NN}}$ = 2.4 –7.7 GeV. Sci. China Phys. Mech. Astron. **66**, 232011 (2023). https://doi.org/10.1007/s11433-022-2041-8

53. R.J. Charity, A Systematic description of evaporation spectra for light and heavy compound nuclei. Phys. Rev. C **82**, 014610 (2010). https://doi.org/10.1103/PhysRevC.82.014610

54. K. Hagel, M. Gonin, R. Wada et al., Violent collisions and multifragment final states in the Ca-40 + Ca-40 reaction at 35 MeV/nucleon. Phys. Rev. C **50**, 2017–2034 (1994). https://doi.org/10.1103/PhysRevC.50.2017

55. J. Su, F.S. Zhang, Isotopic dependence of nuclear temperatures. Phys. Rev. C **84**, 037601 (2011). https://doi.org/10.1103/PhysRevC.84.037601

56. Z.T. Dai, D.Q. Fang, Y.G. Ma et al., Effect of neutron skin thickness on projectile fragmentation. Phys. Rev. C **91**, 034618 (2015). https://doi.org/10.1103/PhysRevC.91.034618

57. Y.G. Ma, R. Wada, K. Hagel et al., Sequential decay distortion of Goldhaber model widths for spectator fragments. Phys. Rev. C **65**, 051602 (2002). https://doi.org/10.1103/PhysRevC.66.029902

58. M. Huang, Z. Chen, S. Kowalski et al., Isobaric yield ratios and the symmetry energy in fermi energy heavy ion reactions. Phys. Rev. C **81**, 044620 (2010). https://doi.org/10.1103/PhysRevC.81.044620

59. L. Li, F.Y. Wang, Y.X. Zhang, Isospin effects on intermediate mass fragments at intermediate energy-heavy ion collisions. Nucl. Sci. Tech. **33**, 58 (2022). https://doi.org/10.1007/s41365-022-01050-w

60. J. Su, L. Zhu, C. Guo, Influence of the nuclear level density on the odd-even staggering in ^{56}Fe+p spallation at energies from 300 to 1500 MeV/nucleon. Phys. Rev. C **97**, 054604 (2018). https://doi.org/10.1103/PhysRevC.97.054604

61. L.M. Liu, C.J. Zhang, J. Xu et al., Free spectator nucleons in ultracentral relativistic heavy-ion collisions as a probe of neutron skin. Phys. Rev. C **106**, 034913 (2022). https://doi.org/10.1103/PhysRevC.106.034913

62. X. Lei, E. Xiao, Y. Feng et al., Production of neutron-deficient nuclei around N= 126 by proton-induced spallation. Chin. Phys. C **47**, 014102 (2023). https://doi.org/10.1088/1674-1137/ac9601

63. Q.F. Song, L. Zhu, J. Su, Target dependence of isotopic cross sections in the spallation reactions ^{238}U + p, d and ^{9}Be at 1 AGeV. Chin. Phys. C **46**, 074108 (2022). https://doi.org/10.1088/1674-1137/ac6249

64. D. Mancusi, R.J. Charity, J. Cugnon, Unified description of fission in fusion and spallation reactions. Phys. Rev. C **82**, 044610 (2010). https://doi.org/10.1103/PhysRevC.82.044610

65. M. Wang, W.J. Huang, F.G. Kondev et al., The AME 2020 atomic mass evaluation (II). Tables, graphs and references. Chin. Phys. C **45**, 030003 (2021). https://doi.org/10.1088/1674-1137/abddaf

66. Z. Gao, Y. Wang, H. Lü et al., Machine learning the nuclear mass. Nucl. Sci. Tech. **32**, 109 (2021). https://doi.org/10.1007/s41365-021-00956-1

67. W. Reisdorf, H.G. Ritter, Collective flow in heavy-ion collisions. Ann. Rev. Nucl. Part. Sci. **47**, 663–709 (1997). https://doi.org/10.1146/annurev.nucl.47.1.663

68. G. Lehaut, D. Durand, O. Lopez et al., Study of nuclear stopping in central collisions at intermediate energies. Phys. Rev. Lett. **104**, 232701 (2010). https://doi.org/10.1103/PhysRevLett.104.232701

69. W. Reisdorf, Y. Leifels, A. Andronic et al., Systematics of azimuthal asymmetries in heavy ion collisions in the 1 A GeV regime. Nucl. Phys. A **876**, 1–60 (2012). https://doi.org/10.1016/j.nuclphysa.2011.12.006

70. A. Andronic, J. Lukasik, W. Reisdorf et al., Systematics of stopping and flow in Au+Au collisions. Eur. Phys. J. A **30**, 31–46 (2006). https://doi.org/10.1140/epja/i2006-10101-2

71. A. Le Fèvre, Y. Leifels, C. Hartnack et al., Origin of elliptic flow and its dependence on the equation of state in heavy ion reactions at intermediate energies. Phys. Rev. C **98**, 034901 (2018). https://doi.org/10.1103/PhysRevC.98.034901

72. O. Lopez, D. Durand, G. Lehaut et al., In-medium effects for nuclear matter in the Fermi energy domain. Phys. Rev. C **90**, 064602 (2014). https://doi.org/10.1103/PhysRevC.90.064602

73. W. Reisdorf, A. Andronic, R. Averbeck et al., Systematics of central heavy ion collisions in the 1A GeV regime. Nucl. Phys. A **848**, 366–427 (2010). https://doi.org/10.1016/j.nuclphysa.2010.09.008

74. W. Reisdorf, A. Andronic, A. Gobbi et al., Nuclear stopping from 0.09 to 1.93-A-GeV and its correlation to flow. Phys. Rev. Lett. **92**, 232301 (2004). https://doi.org/10.1103/PhysRevLett.92.232301